PROCEEDINGS OF SPIE

SPIEDigitalLibrary.org/conference-proceedings-of-spie

Performance testing and end-to-end mapping of the fiber cable on the SALT NIR integral field spectrograph

Joshua Oppor, Matthew A. Bershady, Marsha J. Wolf, Michael P. Smith, Sabyasachi Chattopadhyay, et al.

Joshua Oppor, Matthew A. Bershady, Marsha J. Wolf, Michael P. Smith, Sabyasachi Chattopadhyay, Kurt Jaehnig, Jeffrey Percival, Mark Mulligan, Kathleen Jurgella, Briana Wirag, "Performance testing and end-to-end mapping of the fiber cable on the SALT NIR integral field spectrograph," Proc. SPIE 12188, Advances in Optical and Mechanical Technologies for Telescopes and Instrumentation V, 121885P (29 August 2022); doi: 10.1117/12.2630176



Event: SPIE Astronomical Telescopes + Instrumentation, 2022, Montréal, Québec, Canada

Performance testing and end-to-end mapping of the fiber cable on the SALT NIR integral field spectrograph

Joshua Oppor^{a,*}, Matthew A. Bershady^{a,b,c}, Marsha J. Wolf^a, Michael P. Smith^a, Sabyasachi Chattopadhyay^{b,a}, Kurt Jaehnig^a, Jeffrey Percival^a, Mark Mulligan^a, Kathleen Jurgella^a, and Briana Wirag^a

^aUniversity of Wisconsin, Department of Astronomy, 475 North Charter Street, Madison, WI 53706, USA; ^bSouth African Astronomical Observatory, 1 Observatory Rd, Observatory, Cape Town, 7925, South Africa; ^cDepartment of Astronomy, University of Cape Town, Private Bag X3, Rondebosch 7701, South Africa

ABSTRACT

The optical fiber integral field unit (IFU) built to feed the near infrared (NIR) spectrograph for the 11-meter Southern African Large Telescope (SALT) has undergone prototyping and rigorous performance testing at Washburn Astronomical Laboratories of the University of Wisconsin-Madison Astronomy Department. The 43 m length of 256 fibers which make up the object and sky arrays and spares are routed from the SALT payload down into the spectrograph room in four separate cables. The IFU covers 344 arcsec² on the sky, with the object array spanning a 552 arcsec² near-rectangular area at roughly 56% fill-factor. Companion papers describe the mechanical design of the fiber cable that mitigates potential sources of mechanical strain on the optical fiber (Smith et al.) and details of the spectrograph (Wolf et al.). Here we present the results of the performance testing of various test cables as well as performance testing and end-to-end mapping of the fully-assembled science cable. The fiber optics experience an extreme temperature gradient at the ingress to the instrument enclosure held at -40 °C during operation. We find an increase in focal ratio degradation (FRD) when holding progressively longer lengths of test fiber at reduced temperature. However, we confirm that this temperature dependent FRD is negligible for our designed length of cold fiber. We also find negligible contributions to FRD from the rubber seal that breaches the room temperature strain relief box and the cold instrument enclosure. Our measurements characterize performance including the effects of internal fiber inhomogeneities, stress induced from fiber handling and termination, as well as any imperfections from end-polishing. We present the room-temperature laboratory performance measurements of the fully-assembled science cable; the effective total throughput the fiber cable delivers to the spectrograph collimator is $81\pm2.5\%$ across all fibers accounting for all losses.

Keywords: optical fiber, integral field spectroscopy, NIR spectroscopy, FRD, IFU, SALT, RSS-NIR

1. INTRODUCTION

Fiber-optics have become a popular means to couple telescopes to near-infrared spectrographs both for high-resolution studies of single stellar sources (e.g., NESIE¹, SAND²) and multi-object spectroscopy (FMOS³, APOGEE⁴, PFS⁵, MOONS⁶). None, to date, have been designed for integral-field spectroscopy of extended sources. We have undertaken to build a near-infrared fiber IFU to feed the NIR spectrograph on SALT to do just that. The all-refractive spectrograph ^{7,8} (also described by Wolf et al. in these proceedings) is fully cooled and semi-cryogenic; with the current 900 l/mm volume phase holographic grating it covers 0.8 to 1.7 μm with an articulating camera. Spectral resolution ranges from 2000 to 6000 over this band-pass with the 1.33" fiber optical diameter of our IFU. The band-pass extends the 0.32-0.9 μm coverage of RSS-VIS⁹.

The fiber cable we have designed, fabricated and now installed on SALT, consists of a 212-fiber object array, 38-fiber sky array, and 6 spares. The fibers are 43 m in length and are Molex/Polymicro FIP 300:330:370 step-index multi-mode core and cladding, with polyamide buffer. The object array spans a 29" x 18" elongated hexagonal footprint and can be separated from the associated sky array anywhere from 48.6" to 159.2". The two arrays are mounted into a gimballed jaw at SALT's fiber instrument feed (FIF) which maintains telecentricity as they

Advances in Optical and Mechanical Technologies for Telescopes and Instrumentation V, edited by Ramón Navarro, Roland Geyl, Proc. of SPIE Vol. 12188, 121885P © 2022 SPIE · 0277-786X · doi: 10.1117/12.2630176

are separated at prime focus. The sky array spans a footprint of 18" x 4" and samples the range of telecentric offsets experienced by the fibers in the object array. At the spectrograph, the fibers are arranged in a linear pseudo-slit, 104 mm in length.

Fibers are especially useful for delivering light to an instrument when access to the prime focus is limited, as in the case of SALT. Additionally, SALT has a varying pupil over the course of an observation. For a wide-field imaging spectrograph this can manifest as a spatially and temporally varying line-spread function (LSF), making calibration of both flux and the LSF challenging. The challenge is compounded on a queue-scheduled telescope which must complete many programs with different spectrograph configurations on any given night. The inability to calibrate the LSF well is not only an issue for kinematic measurements, but also for the subtraction of sky-lines that dominate terrestrial near-infrared foregrounds. Fiber-fed instruments are well suited for SALT specifically because they scramble injected light in the near- and far-field, resulting in a considerably more stable LSFs than imaging spectrographs.

Historically, SALT's NIR spectrograph (formerly called RSS-NIR) was to be mounted as second beam on an existing imaging spectrograph – RSS-VIS. To reduce thermal background in the H-band, the initial design had the last collimator group, the gratings and most of the camera in a cooled enclosure held at -40 °C, with the final camera elements and detector held in an additional cryostat 10,11 . This cooling requirement led to such significant weight and complexity at the prime focus payload, with commensurate added risk (e.g., coolant leakage) and increased maintenance cost. In 2014 we therefore switched to a fiber-fed NIR-only spectrograph concept with a superior collimator design; the spectrograph is entirely housed in a -40°C enclosure on the ground level of the observatory. The overall simplicity of the new collimator compared to RSS-VIS, plus the lower emissivity of an entirely cooled spectrograph more than compensates for fiber losses. The detailed routing and mechanical challenges of the cable design are presented by Smith et al. (in these proceedings). Here we focus on the performance attributes of the fibers themselves in the as-built cable. We describe the methods and measurements associated with our performance testing, sources and mitigation of strain, and finally the detailed mapping scheme and performance of the fully-assembled science cable.

2. METHODS AND MEASUREMENTS



Figure 1. Completed NIR fiber cable set up on TSW. Four sections of conduit, each nearly 40 meters long, are spooled in figure-eights on the left.

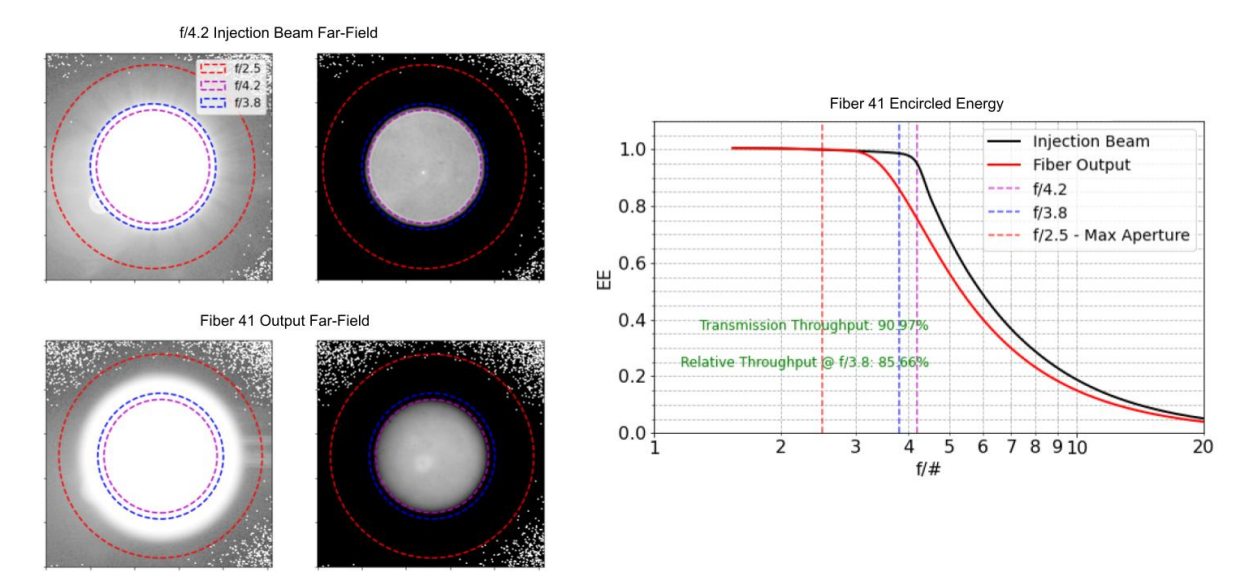


Figure 2. I-band images from TSW along with encircled energy (EE) curves for a fiber in the object array. Top images show the far-field output pattern of the f/4.2 injection beam, scaled logarithmically to show background and core structure respectively. Bottom images show the same for the far-field output of the fiber. Ideally, the injection EE curve should be a parabolic function of f/# with a sharp edge at EE100; because of diffraction and scattering it exhibits a 'soft' edge. We find EE95 at f/4.2 for the injection beam, and we account for this in our analysis.

2.1 Wisconsin Test Stand

We briefly describe the apparatus used to determine optical performance of all test cables and final science cable discussed throughout the rest of this paper. The fiber test-stand at the University of Wisconsin's Washburn Astronomical Laboratories (hereafter TSW) ^{12,13,14} uses a double-differential technique to capture and compare an injection beam to the output beam of a fiber. TSW is equipped with a standard suite of broad and intermediate-band filters, adjustable apertures to tune injection beam speed and additional cameras to precisely place the injection spot on the surface of a fiber. The injection spot is produced by re-imaging a pinhole which sits in front of an evenly illuminated opal diffuser and shows a high degree of uniformity in both the near- and far-field. The pinhole is also swappable to accommodate injection into different fiber diameters without over-filling them. TSW is well suited to systematically test each fiber in the final science cable. We make use of this modular test stand, illustrated in Figure 1, and describe the results in §5.

The differential measurement consists of first collimating the injection beam directly onto an SBIG CCD detector. Then the injection beam optics slide to place the focused beam into the fiber, while moving the fiber output into the same collimating optics and detector. A separate flux-monitoring diode samples the input beam via a dichroic placed before the pinhole, providing the second differential. A small telescope and pellicle setup allows for the precise centering of the injection spot onto the test fiber. A more recent addition is a field stop placed just beyond the intermediate focus of the injection beam, or equivalently just in front of the fiber output face. The field stop, with carefully calibrated placement, mitigates reflections off the surface of some of our ferrules. The test stand is well baffled, and yields high S/N measurements from 400-800 nm. In these tests, an injection beam-speed of f/4.2 is used to simulate the prime focus of SALT. Since I-band light is not visible by eye, the R-band was used to center and calibrate the injection beam manually before subsequently making measurements in the I-band.

2.2 Focal ratio degradation and throughput

Light traveling through optical fibers experiences focal ratio degradation (FRD)^{15,16}. For a point source, a telescope produces a converging beam of uniform surface brightness in the far-field with sharply defined edges corresponding to the telescope primary aperture and any obscurations (in the case of SALT these obscurations include the spherical aberration corrector, and the tracker which carries it and the instrument payload). In contrast, when this beam is imaged onto a fiber, the fiber output far-field light distribution is faster, no longer uniform, and has 'soft' edges. As a result, larger or faster optics are necessary to capture all of the light transmitted through a fiber. The causes of FRD likely include scattering from micro-bends or micro-fractures within the fiber material ¹⁷; mechanical stress due to routing load, bend radius, termination, and surface finish imperfections ¹⁸. As we report here, we also find that thermal gradients can induce FRD.

We use the calibrated plate scales of the TSW measurement engine and Python routines to determine the angular distribution of light within both the injection beam and test fiber far-field. The algorithm determines the center of each far-field pattern and computes encircled energy as a function of beam speed (see Figure 2). We focus on a fiber's encircled output energy within an f/3.8 aperture relative to the total encircled energy of the fiber output since f/3.8 is the spectrograph's collimator speed. We also measure the transmission throughput to assess losses due to material attenuation and surface reflections ($\sim 3.43\%$ per surface). For FIP fiber of 43 m length we expect attenuation losses of 84% at 0.65 µm, 95% at 0.8 µm, 99% at 1.1 µm and 95% at 1.7 µm. Hence peak transmission throughput should be no more than 92%.

2.3 Fiducial performance and prototyping



Figure 3. (Top) Stainless steel single-fiber ferrule with pre-bonded hypodermic needle. (Bottom) Single fiber termination fully strain relieved with heat-shrink tubing.

In order to set a baseline amount of mechanical strain and its impact on fiber performance in the final science cable, several test cables were fabricated. They consist of the same fiber and employ the same epoxy, termination, and polishing techniques used in the instruments final science cable, described below. Two, single-fiber cables (referred to as XC1 and XC3) were terminated in custom single-fiber ferrules designed to minimize mechanical loading and termination strain. XC1 is 3 m in length, while XC3 is 43 m in length. The fiber is bonded over a short (\sim 2 mm) length protruding from a pre-bonded hypodermic needle in the 1/4-cut groove of a steel ferrule as seen in Figure 3. Care was taken to ensure bare fiber does not experience mechanical strain against the rigid edges of the hypodermic needle. Even with these single-fiber ferrules, twisting and improper strain relief results in significant FRD. Graduated layers of heat-shrink tubing transition the fiber from the hypodermic needle into a length of crush-resistant Teflon sleeving. Tests from these single-fiber ferrules set a fiducial transmission throughput and FRD baseline to which subsequent tests are compared. XC1 has a transmission throughput of 94% (consistent with its 3 m length) and relative throughput at f/3.8 of 88% in the I-band. XC1 and XC3 were used to verify the attenuation measurements provided by Polymicro; XC3 was also used to determine thermal strain, described in §4.

An additional test-cable of 60 fibers (XC2, 8m in length) was constructed as a short prototype of one of the four conduits in the final science cables. Fibers were encapsulated each in their own Teflon sleeve held inside a single PVC-coated flexible steel-interlock conduit. (In the final science cable, 64 fibers each 43 m in length are placed in an identical conduit over 40 m in length, again in individual Teflon sleeves). On both ends of the conduit, the fibers emerge and are sorted into rectangular arrays through holes in positioning-plates. These plates also serve to terminate the Teflon; the sleeves are captured via an adhesive-heat-shrink bond. An earlier attempt to use a sheer clamps to anchor the Teflon sleeves proved unworkable since the sleeves were not sufficiently over-sized (as they had been in our previous long-cable IFUs ^{12,19}) to avoid significant FRD-inducing stress into the fibers. The entire junction junction is referred to as a break-out box, illustrated in Figure 8. The heat-shrink anchors were prototypes for application on the final science cable; the prototyping was invaluable to establish our application technique. From the break-out box to the final fiber termination the fibers are routed in groups through furcation tubing. One fiber per V-groove block retained their Teflon sleeving to test if this further minimized strain (FRD), an important point that we return to in §3.3.

XC2 had a variety of terminations used to test the impact of these terminations on fiber performance (see §3.1), and to test mechanical longevity of the fiber cable to actuation on the telescope during the lifetime of the instrument (see §3.3, Video 1). At the end of these prototyping exercises, XC2 was re-terminated to serve as the test and integration cable (TIC) for the spectrograph (§3.4).

3. TERMINATIONS AND MECHANICAL STRAIN

During cable design and assembly our main concern was to understand and mitigate various sources of mechanical strain along the length of the fiber. Below we describe our choice of epoxy and methods for bonding fibers into V-groove blocks or U-channel blocks. We also discuss the effects of polishing and surface finish on FRD. We close this section with a discussion of long-term mechanical strain and performance testing of the test and integration cable (TIC), a precursor to the final science cable.

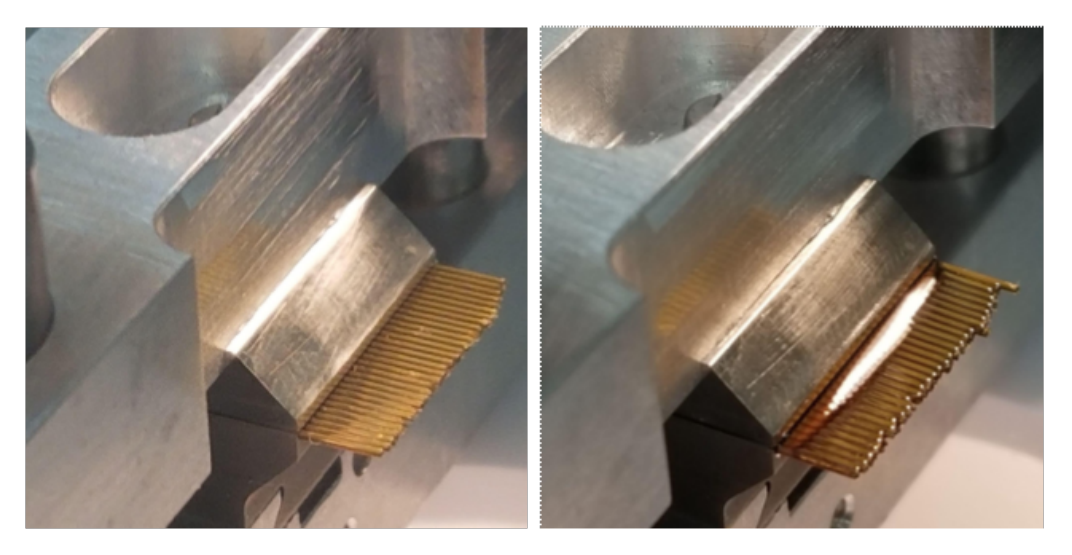


Figure 4. (Left) V-groove block with well-seated fibers and (Right) after epoxy application.

3.1 Epoxy termination

Epo-tek 301 two-part epoxy was used to bond fibers into their respective ferrules. A recipe for epoxy application was developed to ensure optimal viscosity (to prevent undue wicking which can lead to increased FRD and breakage) while reducing the number of bubbles present in the epoxy at the time of application (bubbles compromise the rigidity of the optical surface). This epoxy was chosen to match the coefficient of thermal expansion (CTE) of the fiber fused silica and the invar used to fabricate the V-groove blocks which make up the pseudo-slit end

of the fiber cable. However, it was also used for all fiber terminations. For the invar V-groove blocks, epoxy and glass, CTE is minimal between room temperature, the environment in which the V-groove blocks are assembled, and -40 °C operating environment. This choice of epoxy and application recipe appears to mitigate significant mechanical strain that may have been induced immediately at these terminations. We did find, however, that different batches of the same epoxy could vary in pre-cure time for a given viscosity. As a result, each prepared batch of epoxy was tested before application to the final science cable. These tests involved tracing the viscosity and bubble content as a function of pre-cure time. The final science batch of epoxy ended up having a pre-cure time of about 3.5 hours, 0.5 hours shorter than the initial batch of epoxy used to develop the recipe.

3.1.1 V-groove bonding

After 30 to 32 fibers (depending on the V-groove block's pseudo-slit position) were cut to length and laid across a 13 mm V-groove block, a precise amount of epoxy (0.01 mL) was applied along the leading edge, just under the V-groove block lid. This application, combined with the pre-cured viscosity prevent excessive wicking and minimizes the presence of bubbles at the polishing surface. The lid is gently pressed down on the top of the V-groove block to properly seat the fibers using a custom jig, illustrated in Figure 4. A depth gauge on either side of the gluing jig is used to ensure uniform pressure. The seating of fibers in the V-groove blocks is shown in Figure 7. The initial layer of epoxy is allowed 24 hours to cure, then a second 'buffer' layer is added to ensure coverage around the edge fibers protruding from the end of the V-groove block. This provides mechanical stability during polishing. Without a buffer of epoxy there is a chance that fibers can chip or splinter during the polishing process. A similar strategy was employed for the epoxy bonding of the object array and sky array into U-channel blocks described below.

To ensure the V-groove bonding process did not degrade fiber performance we initially terminated two fibers of XC2 into single ferrules (as done for XC1 and XC3) on both sides and tested performance. Then, the two fibers were re-terminated into either edge of a V-groove block on one side and re-tested. No increase in FRD was noted for these two fibers between the different terminations, indicating no substantial degradation in performance due to the V-groove termination given our V-groove termination process (including lid pressure).



Figure 5. (Left) Use of 3D printed fiber brackets designed to hold rows of 17 or 18 fibers in our mapping (§5.1). Row-sorted fibers, captured by these brackets, fill the IFU U-channel mount. (Right) A gluing jig and guide U-channel were used to aid in the termination of the object and sky arrays.

3.1.2 IFU bonding

Fibers were sorted into rows, captured using 3D-printed brackets, then layered on top of one another to fill the U-channel forming the IFU mechanical block (Figure 5. The U-channel, cut using wire EDM, was tested to fit 18 fibers side-by-side with minimal gaps). Once every row was properly seated, a small piece of 60 µm shim stock was inserted under the fastened lid of the U-channel. Fibers were then fanned out and 0.01 mL of epoxy was applied to the top of each row in front of the U-channel. An additional 0.01 mL was applied along the outer edges of the array of fibers. The fibers were then retracted into the U-channel to ensure epoxy contact between each fiber, the walls of the U-channel, and lid without allowing for wicking out the back of the U-channel block. This method was used to terminate the IFU on TIC and did not show increases in FRD when fibers were

re-terminated from the XC2 configuration (single ferrules on one side and V-groove blocks on the other as the test described in § 3.1.1) into the TIC configuration (V-grooves on one side and IFU on the other).

3.2 Polishing

All fiber cables were polished to the same degree using silicon-carbide (SiC) lapping paper and a custom rotary polisher ²⁰. The setup and polishing engine are shown in Figure 6. After termination, ferrules are first polished by hand with 280-grit sandpaper to within 100 µm of the nominal focal surface. Then, a nearly consistent recipe for polishing was determined using 60, 30, 15, 5, 3, 1 and 0.3 µm lapping paper to bring the surface finish to completion.

Table 1. Ferrule types, surface areas, and optical to mechanical surface-area ratios

Ferrule Type	Optical Area (mm ²)	Mechanical Area (mm ²)	Area Ratio (%)
Single Fiber Ferrule	0.1	3	3
V-groove Block	4	30	13
Sky Array	7	26	27
Object Array	29	56	52

Table 2. Ferrule types, polishing speed and load up to the 3μm polishing step and finer than the 3μm polishing step.

Ferrule Type	Speed $> 3\mu m \text{ (RPM)}$	$Load > 3\mu m (g)$	Speed $< 3\mu m (RPM)$	$Load > 3\mu m (g)$
Single Fiber Ferrule	600	150	<100	150
V-groove Block	600	150	< 100	150
Sky Array	600	150	< 100	50
Object Array	600	150	< 100	30

Polishing a single fiber in a ferrule is easier than polishing a 1D array of fibers in a V-groove. Polishing a 2D array of fibers in a U-channel block is harder still. The difficulty is largely a function of surface area. For our cable build and prototyping the surface areas of different ferrules are given in Table 1. Despite the differences in glass surface area, mechanical surface area and the ratio of glass to mechanical surface area, we found a consistent polishing recipe (load and speed) brought each ferrule type to a similar level of surface finish at coarser grits (>3 µm). This actually implies a decreasing pressure with increasing total surface area. At finer grits, while the speed remained consistent, the load had to be decreased further as a function of increasing optical area. Table 2 gives a summary of this polishing recipe. Combined with Table 1 it is clear that both optical surface area and optical to to mechanical surface area ratio are important considerations.

The V-groove blocks and U-channel blocks were polished using 600 RPM and 150 g on the load cell seen in Figure 6 for the 60, 30, 15 and 5 µm polishing steps. At 3 µm and finer steps, subtle skipping on the platen can be heard indicating that, despite significant effort to level the polishing platen, the surface is not adequately flat. (The platen is made of hard-anodized aluminum; in the future we intend to explore application of fused-silica surfaces). We found that when polishing too quickly, new scratches were easily produced, in part, because of this skipping. Hence at the 3 µm polishing step and finer, the platen was rotated at a much slower rate (< 100 RPM). In the case of larger ferrules (e.g. the object and sky arrays) significantly less pressure was applied. In these cases we found that the lapping paper would quickly get destroyed with 150 g load and had to drop to 50 g to 30 g load for lapping paper 3 µm and finer.

In addition to polishing more slowly and with less pressure, all ferrules were carefully placed on the same section of the platen (in radius and azimuth with respect to the center of the platen) using a series of hard stops and articulating polishing arm. We chose to keep the ferrules at a radius of about 80 mm from the center (out of a maximum platen radius of 100 m), and aligned on a tangent at this radius (this reduces the instances where the lapping paper comes in contact with metal before the optical surfaces). Finally, a ferrule is never placed down

on an already used section of lapping paper; the lapping paper is replaced before each pass to reduce particulate damage. Examples of the polishing process are shown in Figure 7.

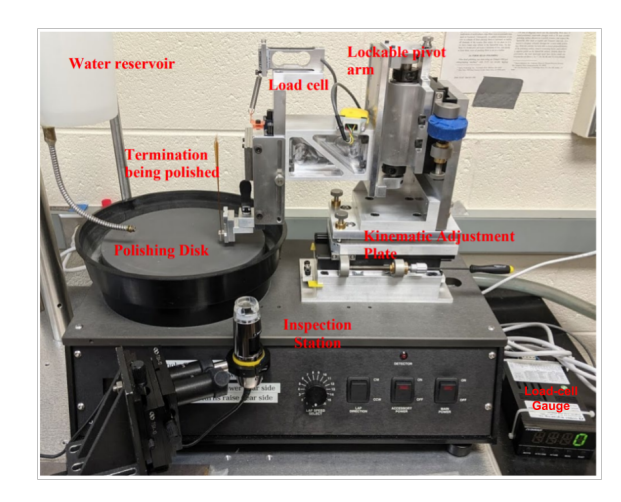




Figure 6. (Left) Custom polisher with inspection microscope which uses two illumination modes to characterize the quality of surface finish. The circumferential illumination mode is especially useful for detecting digs in the surface of a fiber whereas the axial illumination mode seems to be more sensitive to light scratches especially when polishing with very fine lapping paper. (Right) Object array being polished on our custom polisher. The sky array is underneath the tripod awaiting its turn. Any ferrule must be brought to completion before removing it from the polisher in order to prevent faceting.

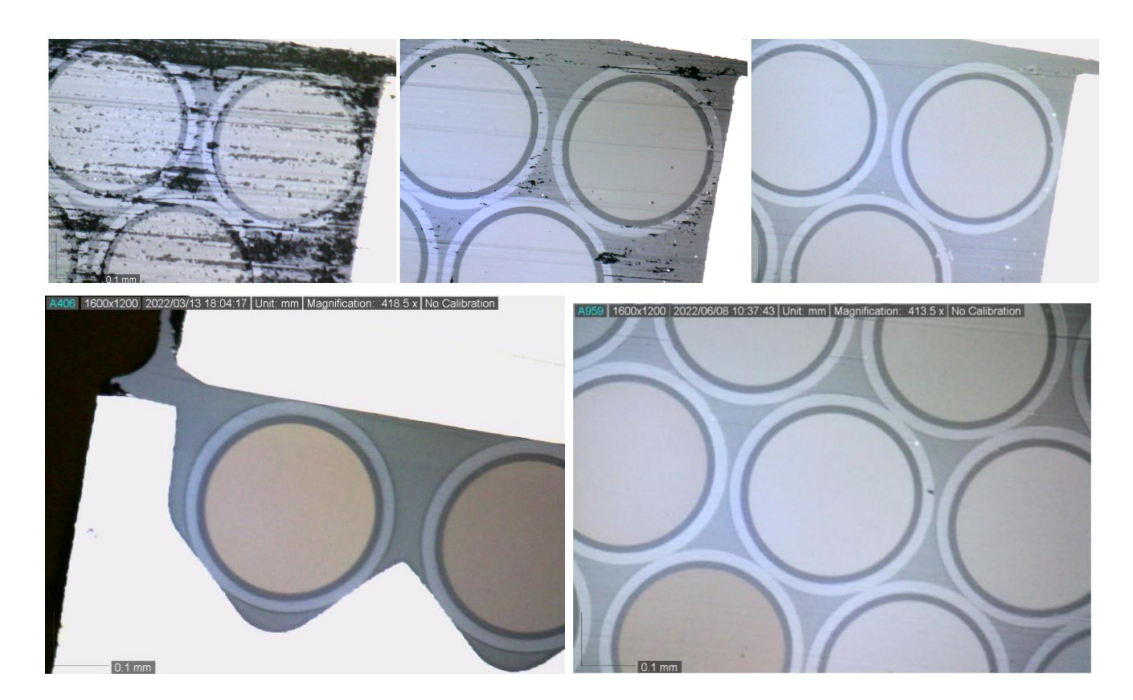


Figure 7. (Top row) The sky array during polishing. Left to right: surface finish after 15 μ m, 3 μ m, and 0.3 μ m lapping paper polishing. The lid is not in contact with the top of each fiber because there is a 60 μ m shim set 5 mm back from the front of the U-channel. (Bottom row) At left are edge fibers terminated in a V-groove block and polished with 0.3 μ m lapping paper. Our method of terminating these V-groove blocks with a gluing jig successfully seats each fiber in its V-groove with full contact on both sides of the V and with the lid. At right is a central portion of the object array after 0.3 μ m polish.

3.3 Fiber cable longevity



Video 1. A short clip of XC2 mounted into the pneumatic actuator meant to simulate the rho-axis rotation of the tracking payload at the prime focus of SALT. http://dx.doi.org/doi.number.goes.here

One fiber-cable routing requirement on SALT is that it must pass through a large cable chain that actuates with the rho-axis rotation of the tracking payload. This actuation occurs regularly during telescope use. We constructed a miniature version on an optical bench in the lab which used an e-chain with identical bendradius, actuated with a compressed-air pneumatic piston. XC2 was configured through the cable-chain and then mounted on TSW to monitor fiber performance before, during and after actuation cycles. 85,000 cycles were used to determine the effects of repetitive mechanical strain over an estimated 10-year lifetime of telescope motion. Video 1 shows the setup and several actuation cycles with XC2 installed. While the detailed distribution of light as a function of angle changed minutely (i.e., mode-scrambling evolved as a function of number of cycles), FRD and total throughput were largely unaffected. In short, this test indicated that the Teflon-sleeved fiber inside the flexible steel-interlock conduit provides robust housing for high-performance fiber-optic cabling.

3.4 Test-and-integration cable (TIC)

After prototyping and testing, XC2 was converted into what is referred to as the test-and-integration cable (TIC). TIC was invaluable in the lab and then again at the telescope to verify optical alignment and performance of the spectrograph prior to the installation of the final science cable. TIC consists of a full set of eight, partially populated V-groove blocks on one side, and a densely packed U-channel block (a prototype IFU) on the other. Within each of the eight V-groove blocks that make up the pseudo-slit, fibers were arranged into a contiguously populated group of six or seven fibers and then an additional fiber positioned with a gap between other active fibers (the fibers placed at a gap from the contiguously packed fibers are referred to as the sparsely populated fibers, and are also those fibers which retained their Teflon sleeving through the furcation tube routing). Between active fibers in each V-groove block, short packing fibers were placed for mechanical integrity. Fiber termination and polishing followed our recipe described in § 3.1.1, § 3.1.2 and § 3.2 above. The densely populated portion of each V-groove block allowed us to measure cross-talk on the detector, while the sparsely populated fibers provided a means to measure scattered light; they were arranged in the prototype IFU so they could be illuminated separately or simultaneously using a manual shutter placed in a telecentric light-feed designed specifically for TIC. The TIC light-feed used an integrating sphere and commercial NIR-optimized aspheric achromats, with an internal pupil stop to set the beam-speed at f/4.2, again, to simulate the beam SALT will deliver. Light was injected outside our instrument cold-enclosure, the TIC then entered the enclosure via a temporary feed-through, and traversed to a prototype fiber pseudo-slit assembly utilizing several 3D printed components.

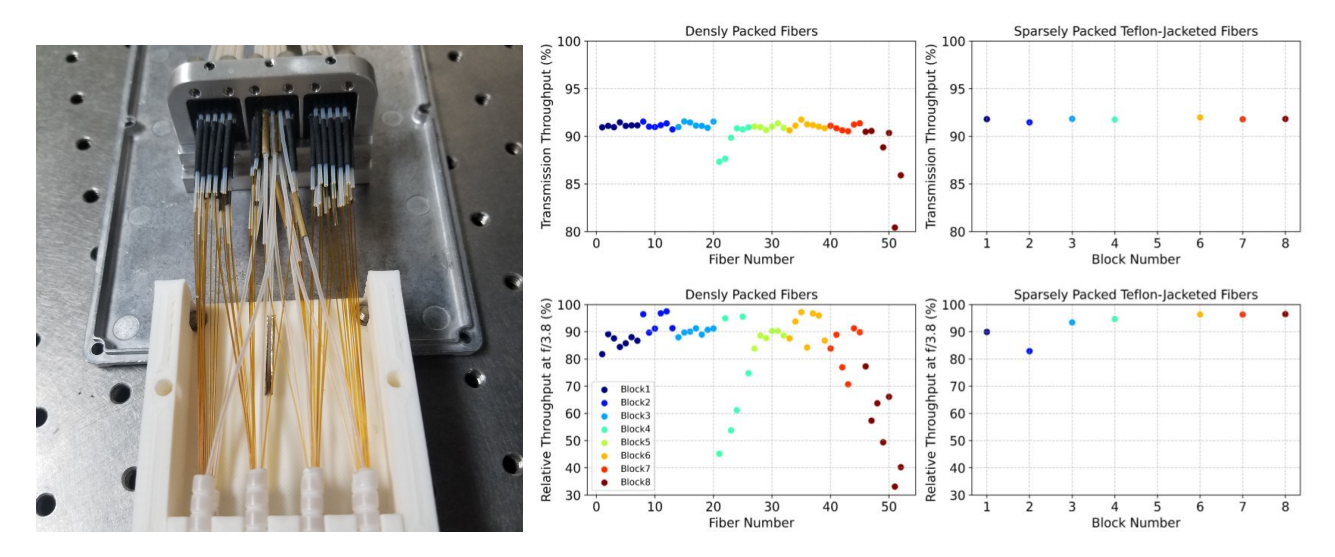


Figure 8. (Left) TIC break-out box, where fibers emerge from the conduit and are separated into 8 groups for termination into V-groove blocks after their Teflon sleeves are terminated. We found that the white furcation tubing (seen at the bottom) caused undue stress on bare fiber, leading to increased FRD. (Right) Throughput and FRD measurements for the TIC. The drop in performance in V-groove block 4, 7 and 8 is not due to polishing imperfections, but rather to the furcation tubing.

Before using TIC on the spectrograph, we measured the throughput of all 60 active fibers on TSW, as shown in in Figure 8. We found that some of the fibers suffered from significant throughput loss due to FRD. We traced this back to mechanical strain introduced by the furcation tubing, which was subsequently eliminated from the final science cable design. We also found that despite the problems with the furcation tubing, those fibers which are Teflon-sleeved inside the furcation tubing performed well which informed our decision to maximize Teflon coverage of the fibers over as much length of the final science cable design as possible.

4. THERMAL STRAIN

The 43 m final science cable reaches the spectrograph cold enclosure via a strain-relief box designed to take up changes in length of fiber from daily temperature changes as well as from mechanical motions of the telescope. Inside the the strain-relief box the Teflon sleeving is removed for roughly a 1 m length of loop. Immediately following, the fibers are re-sleeved in Teflon and reach an air-tight thermal seal that transitions them into the instrument enclosure. The assembly of the thermal seal for the final science cable is shown at the right of Figure 9. The thermal seal feed-through is comprised of two-stages: (i) an outer warm side consisting of layers of 40 Durometer ('00' shore scale) smooth Sorbothane; and (ii) an inner cold side consisting of layers of softer, sponge-like EPDM. Fibers lay across the layers of rubber and are compressed to form a seal within the instrument enclosure wall. A second short gap in the Teflon allows the outer warm Sorbothane to compress around the fibers and seal the Teflon tubing. In this way condensation is prevented from forming inside of the Teflon sleeving while keeping a cold seal than minimizes thermal background seen by the spectrograph. The fibers remain sleeved in Teflon once inside of the spectrograph cold enclosure until they terminate on the slit-plate, whereupon they travel in smooth guide-channels to invar V-groove blocks where they are bonded with CTE-matched epoxy (discussed in § 3.1). Given this journey, the key thermal stress points are the transition of the fiber through the thermal seal and the length of fiber held at -40 °C. We tested both stress points.

4.1 Cold length tests

During the design phase of the science cable it was unclear what length of fiber would be required inside of the cold enclosure. A separate measurement engine was built that uses an opal diffuser, pinhole and a 'source' fiber to produce a fast, uniform beam within a compact format (much smaller than TSW). Use of the source fiber also allows the injection stage to be separated from the rest of the apparatus (see discussion below). A set of



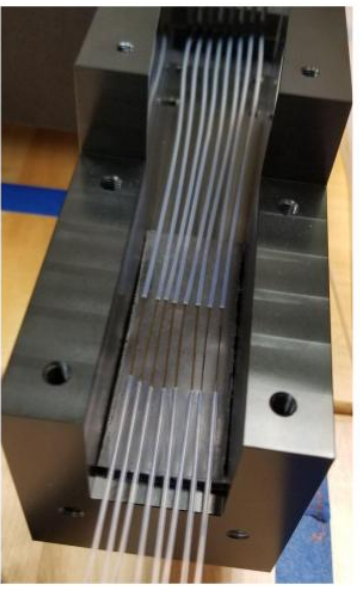


Figure 9. (Left) Test setup using a 3D printed temporary feed-through and the Tenney cold-enclosure. Although the 40 Durometer Sorbothane became significantly more rigid on the inside portion held at -40 °C, no significant FRD was observed. (Right) Teflon-sleeved fibers with a gap of bare fiber which lies across the warm Sorbothane side of the two-stage thermal seal used for the final science cable assembly.

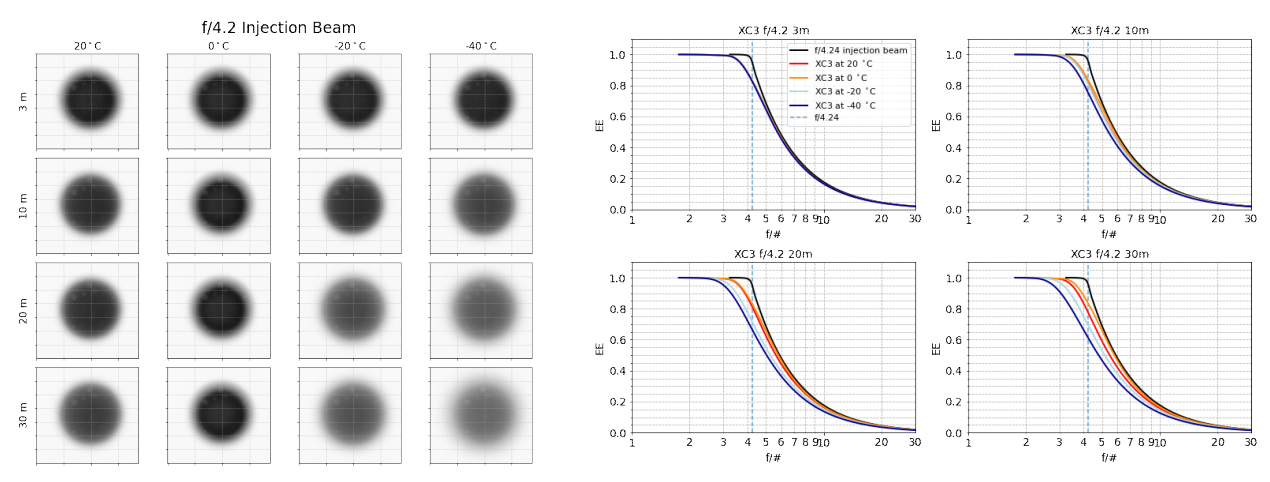


Figure 10. (Left) Far-field images and (Right) their respective encircled energy curves. The flux distribution becomes broader as a function of cold fiber length and decreasing temperature. Colors indicate fiber temperature. A clear increase is FRD is seen at progressively lower temperatures for lengths of fiber held cold at 10 m and longer.

50 mm and 55 mm diameter fast, compound commercial lenses, each with an internal adjustable iris, re-image the diffuser-illuminated pinhole onto the source fiber with a precise f/2.2 beam (the numerical aperture of the source fiber). On a separate stage, the source fiber output was then re-imaged with a fast (f/1.2) 25 mm diameter aspheric achromat and stopped down with an adjustable aperture to form the f/4.2 injection beam. This injection beam was calibrated by capturing the output cone and measuring its EE95 diameter at multiple back-distances with a bare-chip CMOS detector. With the source fiber design this injection stage has the capability to feed a test fiber from within, or outside the Tenney cold-enclosure.

Early phases of cold testing utilized XC1. Since XC1 was only 3 m in length, the injection stage had to lie *inside* the Tenney cold-enclosure (hence the utility of an independent source-fiber injection stage). These measurements did not show additional FRD due to the temperature gradient across its single-fiber termination. We used this setup to also check if FRD was accentuated at the invar V-groove block terminations of XC2 (before it was reconfigured into TIC). We found no evidence for additional FRD.

To determine if there was any dependence of FRD on fiber length held in a cold environment we then tested XC3 (43 m in length) with this setup in our Tenney cold-enclosure. In this case the same measuring apparatus was used in a slightly different configuration. After injection-beam calibration, the injection spot was centered on the the optical surface of the XC3 fiber input *outside* the Tenney cold-enclosure using a pellicle and additional re-imaging camera. XC3 was then routed into the Tenney cold-enclosure where various lengths (3, 10, 20 and 30 m) are neatly and consistently coiled before exiting the freezer. The same bare-chip CMOS camera used to calibrate the injection beam-speed is placed on a separate stage also *outside* the Tenney cold-enclosure and used to capture the entirety of the XC3 output beam. Using similar back-distance measurements in the diverging output cone of XC3, the distance from XC3 to the CMOS detector was determined, allowing for encircled energy measurements similar to those made using TSW data.

The results of our experiment using XC3 are shown in Figure 10 and 11. The FIP fiber experienced a higher degree of FRD both as a function of temperature and as a function of the length of fiber being held cold. Any length longer than about 3 m experienced accentuated FRD below 0 °C. Indeed, these results imply that FRD may be reduced by holding fiber at temperatures around 0 °C. However, at or under 3 m in length, additional FRD is negligible even at temperatures as low as -40 °C. Consequently the length of fiber traversing the inside of the cold enclosure has been limited to under 3 m.

We find further evidence that the impact of thermal strain on FRD is even more pronounced at slower beam speeds, consistent with the general behavior for FRD. These results, as well as comparable tests on FBP-type fiber and fiber of different core:cladding:buffer dimensions, will be reported elsewhere.

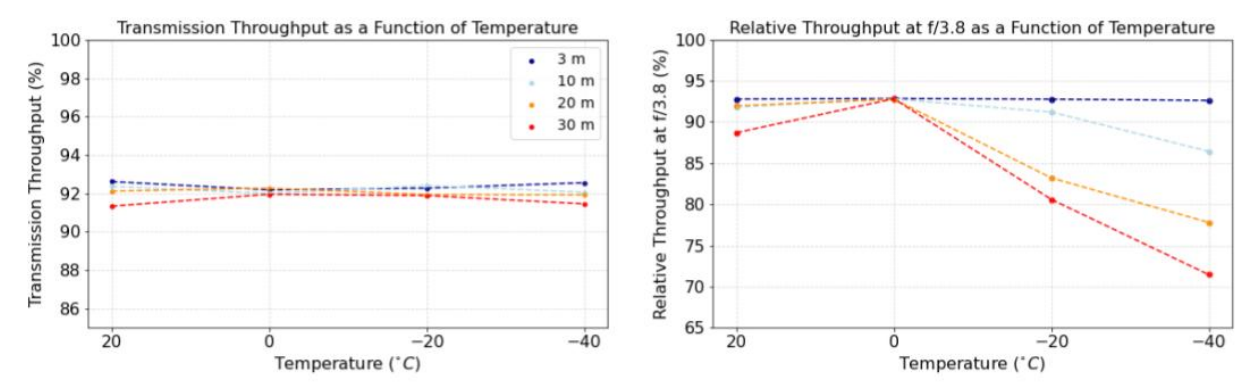


Figure 11. Fiber transmission and FRD as a function of temperature. Colors in these plots indicate fiber length. On the left, a trend in transmission throughput can be seen as a function of length. This is to be expected as more light is attenuated through more material. Transmission throughput remains unaffected as a function of temperature, while FRD worsens below 0° C. While FRD at room temperature is the same within the error of our measurements, the 30-m length sees worse FRD. This is likely a result of the handling or routing of the fiber during the experiment.

4.2 Feed-through rubber seal

XC3 was also used to test the rubber seal required for entrance into the final instrument enclosure. The test article is shown in the left panel of Figure 9. We found that additional FRD was negligible when sufficient pressure to create a seal was applied.

5. FINAL SCIENCE CABLE

5.1 Mapping and non-telecentricity

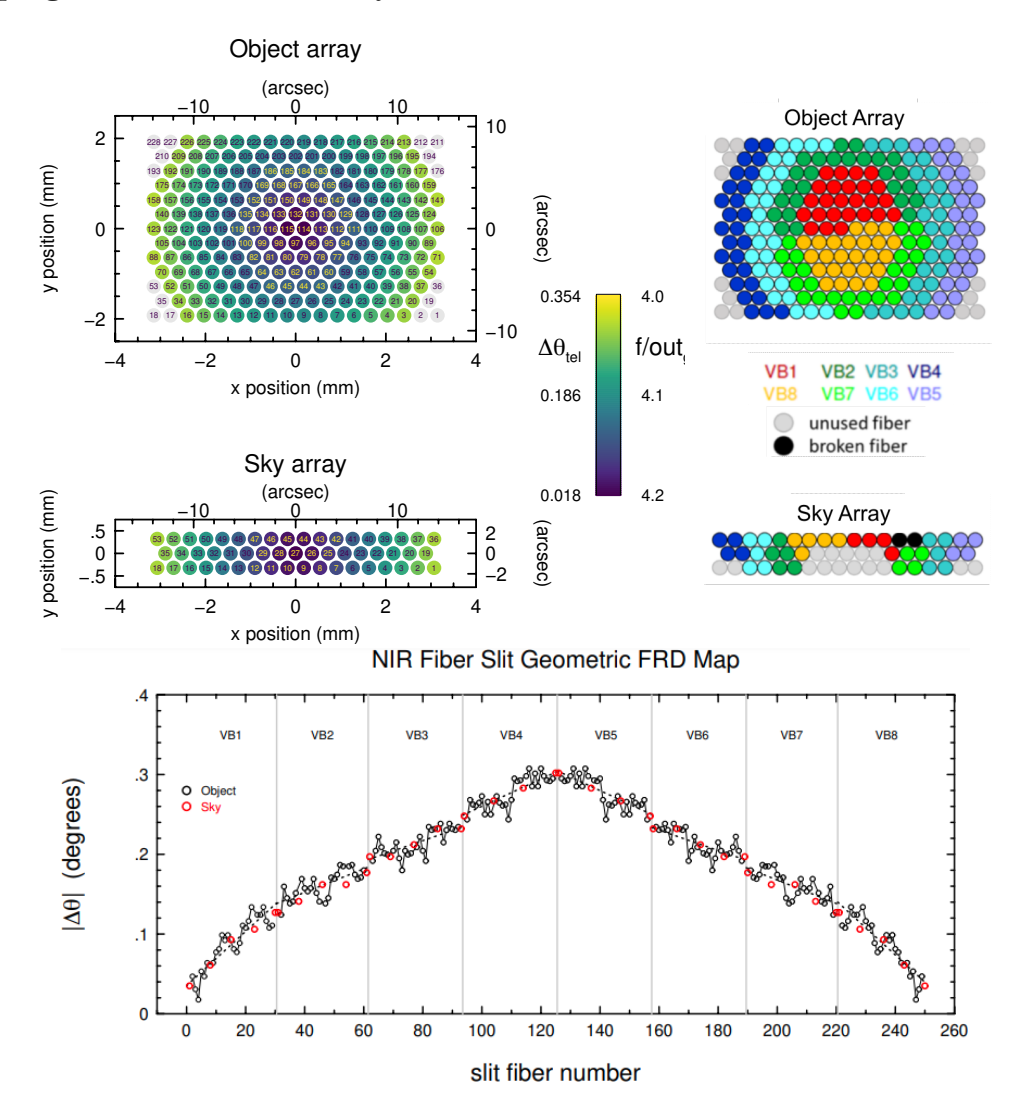


Figure 12. (Top left) Distribution of non-telecentricity for the object array and sky array respectively. Each fiber is color coded by the magnitude of non-telecentricity of the light injection they will receive in the SALT focal plane. Numbers inset inside each fiber are the running fiber number used in fabrication; 1-228 in the object array and 1-53 in the sky array . Inactive (packing) fibers are grey. (Top right) Arrangement of object array and sky array fibers into 8 sections mapping to 8 V-groove blocks. The colors denote different V-groove blocks. (Bottom) Slit function for the variation of the non-telecentric angle ($\Delta\theta$) incident at the telescope focal plane for object array and sky array fibers. Object array fibers are shown as open black circles connected by a black solid like. The red open dots show the allocation of the 38 sky fibers, distributed throughout the slit.

The focal plane of SALT is flat but non-telecentric with a focal ratio of f/4.2. Telecentricity varies by 78" per arcsec on sky from the field center. Fibers at the center of the IFU therefore experience light injection at f/4.2, fibers further from the center experience light injection at beam-speeds as fast as f/4, or a difference in angle up to 0.354 degrees. This geometric effect, illustrated in Figure 12, likely will yield systematic variations in the total effective throughput and the LSF delivered by the spectrograph (due to variations in far-field illumination). While these variations are expected to be subtle, the mapping of the IFU into the slit takes into account these and other performance considerations:

- 1. The range of non-telecentric angles is as small as possible within each of the 8 V-groove blocks in order to maximize sky-subtraction performance by minimizing changes in the LSF due to changes in the injection beam speeds from the fibers.
- 2. The change in non-telecentric angle is a smooth function of slit position within and between the 8 V-groove blocks. This is also to maximize sky-subtraction performance by removing discrete jumps between fibers in their injection beam speeds.
- 3. Fibers in the center of the object array map to fibers at the edges of the pseudo-slit (V-groove blocks 1 and 8) whereas fibers further from the center are mapped to the central V-groove blocks of the pseudo-slit (V-groove blocks 4 and 5). This is to balance S/N between the inner and outer regions of the object array, since galaxies tend to have central light concentrations.
- 4. Fibers adjacent within each V-groove block are mapped to be adjacent to one another in the IFU to minimize the impact of cross-talk above and beyond the beam-smearing introduced by seeing.
- 5. Fibers in the sky array sample as closely as possible the distribution of non-telecentric angles found within the object array. Sky fibers are placed evenly throughout each V-groove block across the pseudo-slit, with non-telecentric angles matching that of the object array fibers in that block. These considerations are designed to improve sky subtraction performance by providing 'local' sky fibers on the pseudo-slit. By 'local' we mean that the fibers share similar input illumination angles and their emergent beams traverse similar paths through the spectrograph optics.

5.2 Final IFU assembly

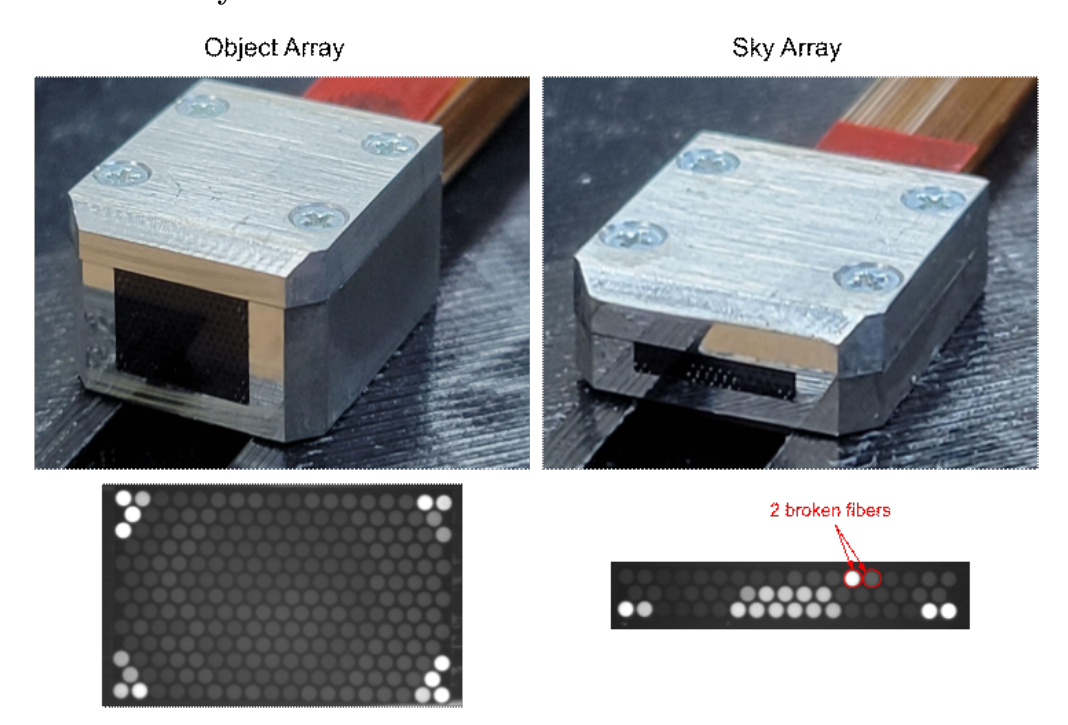


Figure 13. (Left) Object array and (Right) sky array. The red shim from fabrication can be seen attached at the back of each unit. Two sky fibers were broken during fabrication, labelled here. The sky array is symmetric so each non-telecentric angle is still sampled at least once and typically twice.

Fibers are arranged into rows according to the mapping parameters described above and carefully layered into a stainless-steel U-channel block before epoxy application (see Figure 5). With this technique, gaps of order <5 \text{µm} can be seen on the left and right sides of the central fiber as in Figure 7). In the gluing process, a shim

is positioned at the top of the U-channel (see Figure 13) to ensure a snug fit. Consequently any tolerance in the depth of the U-channel is thus shifted into tolerance in the horizontal direction. Fibers along the edges of the U-channel are in contact with the walls in every case.

Twelve of the 228 fibers in the object array switched positions with their neighbors, all within the same row of the array (row 5, up from the dovetail side of the U-channel block). This was caused by a malfunction in a 3D printed fiber bracket used to sort and subsequently bond fibers in place. The impact of these mislocated fiber positions is expected to be minimal since most of the fibers affected remain within their intended V-groove block or an adjacent V-groove block.

Two of the sky fibers broke during final assembly of the sky array. They are located in V-groove blocks 1 and 7. While spare fibers were available, delivery schedule did not allow for sufficient time to re-terminate the sky array. Because these blocks have 4 active sky fibers remaining we do not expect this loss to have a significant impact on the overall performance.

5.3 Final science cable performance

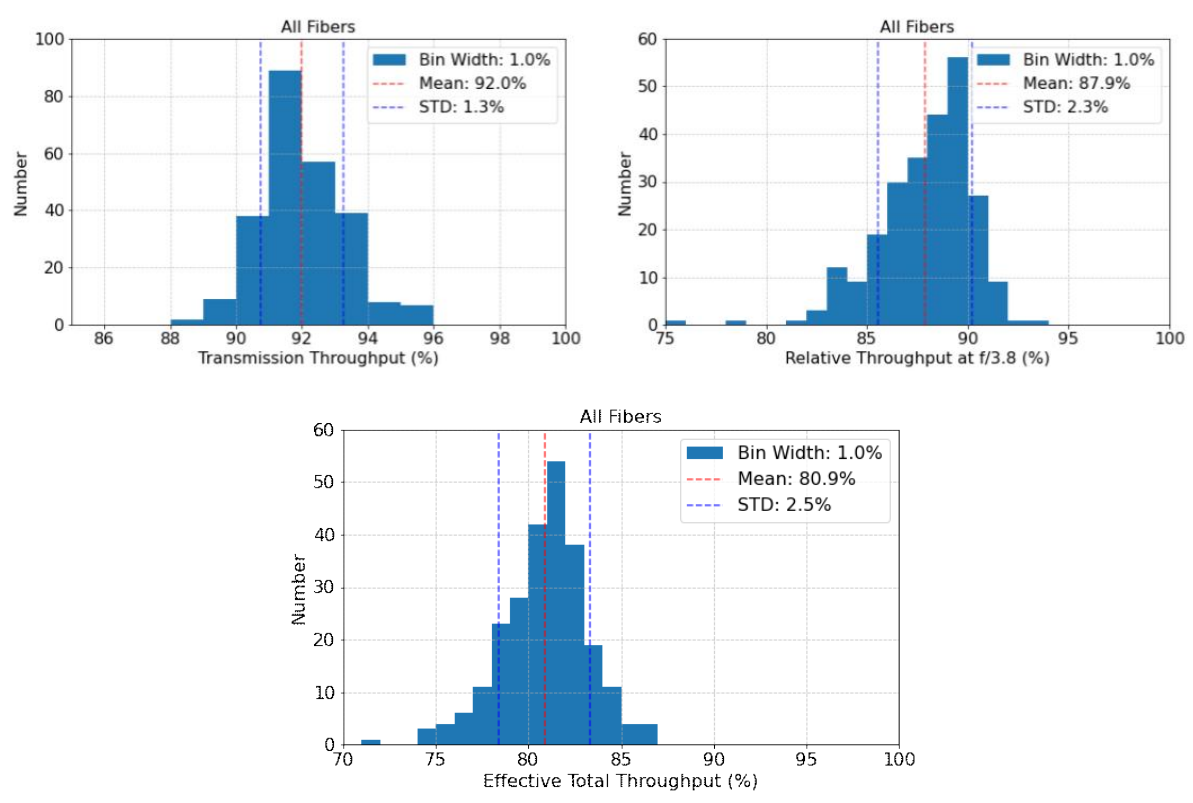


Figure 14. (Top row) (Left) Transmission throughput and (Right) relative throughput at f/3.8 for all 248 active fibers. Distribution standard deviations are due to variations in surface finish and fiber routing stress. (Bottom row) Effective total throughput delivered to the collimator of the spectrograph with an f/3.8 aperture for all 248 active fibers. These values are the product of the transmission throughput and the relative throughput at f/3.8 for each fiber.

All 212 object array fibers and 36 sky array fibers were tested on TSW in the *I*-band with a near-field injection spot of 6.25% fill-factor of the fiber optically active surface. Subsets of fibers were tested using a larger injection-beam spot, with a 69.4% fill-factor. These measurements yielded results within the TSW systematic error of the initial (low fill-factor) measurements. The systematic error in these measurements is of order 1%, primarily due to the presence of internal reflections within the TSW apparatus. Most of these reflections are a consequence of the

commercial, compound camera lens in TSW used as the final collimator in the output module; the optic is non-optimal for use in the I-band, e.g., in the R-band the reflections are dramatically reduced. This is exacerbated, particularly for the V-groove blocks, by reflections off of the highly polished invar surfaces only some of which are block by the field-stop described in § 2.1. These reflections are readily apparent in the logarithmically stretched images found in Figure 2 that accentuates the background counts. Despite these imperfections, the effect on the encircled energy is very small.

Histograms of transmission throughput, relative throughput at f/3.8, and effective total throughput delivered to the collimator of the spectrograph can be seen in Figure 14. The transmission throughput is 92% on average with a very low scatter (1.2%); this is a combination of surface-losses and attenuation. A slightly more significant loss comes from FRD such that on average $\sim 88\%$ of the transmitted flux injected within f/4.2 emerges within f/3.8. However, the scatter is not much larger (2.3%), indicating that the fibers in the final science cable are uniformly strain-relieved. These two efficiency factors yield a total effective throughput within f/3.8 of $\sim 81\%$ on average with a small standard deviation of 2.5% that is essentially the quadrature sum of the scatter in transmission and aperture (FRD) loss, indicating the two are not well correlated.

6. SUMMARY

The tests conducted with our suite of test cables, namely XC1, XC2, XC3 and finally TIC led to the fabrication of a final science cable with average fiber performance similar to that of our fiducial, minimal-strain single-fiber terminations. These tests included our choice of epoxy, methods for bonding fibers into V-groove blocks or U-channel blocks, and the quality of surface polish. We also were able to confirm that (i) our cable design can handle the long-term mechanical actuation required for routing and operating on SALT; and (ii) the thermal gradient necessary to route the fiber cable into the instrument enclosure does not introduce significant increases in FRD.

The fiber cable is now fully routed and installed on SALT and the NIR spectrograph, with first-light reported in these proceedings by Wolf et al. On-sky commissioning is expected to begin within the next few months once relevant telescope sub-systems are ready. One of the first commissioning tests we anticipate is to measure the trends and scatter in effective total throughput of each fiber as a function of slit position and corresponding location in the IFU via continuum flat-field illumination with the SALT calibration system and twilight flats. Differences between these measures and our laboratory calibration will allow us to determine any changes in the mechanical stress of the fiber optics with the cable in situ and during telescope operation.

ACKNOWLEDGMENTS

Support for this research has been provided by NSF/AST-1814682 and the South African National Research Foundation SARChI-114555.

REFERENCES

- C. Kintziger, G. Rauw, R. Desselle, et al., "NSIE: a fiber-fed near-infrared spectrograph for TIGRE telescope," in Ground-based and Airborne Instrumentation for Astronomy VII, C. J. Evans, L. Simard, and H. Takami, Eds., Society of Photo-Optical Instrumentation Engineers (SPIE) Conference Series 10702, 107024Y (2018).
- [2] A. Takahashi, T. Kotani, J. Nishikawa, et al., "The South Africa Near-Infrared Doppler (SAND) instrument: concept and instrument design," in Society of Photo-Optical Instrumentation Engineers (SPIE) Conference Series, Society of Photo-Optical Instrumentation Engineers (SPIE) Conference Series 11447, 114473E (2020).
- [3] M. Kimura, T. Maihara, F. Iwamuro, et al., "Fibre Multi-Object Spectrograph (FMOS) for the Subaru Telescope," 62, 1135–1147 (2010).
- [4] J. C. Wilson, F. R. Hearty, M. F. Skrutskie, et al., "The Apache Point Observatory Galactic Evolution Experiment (APOGEE) Spectrographs," 131, 055001 (2019).

- [5] N. Tamura, N. Takato, A. Shimono, et al., "Prime Focus Spectrograph (PFS) for the Subaru telescope: ongoing integration and future plans," in Ground-based and Airborne Instrumentation for Astronomy VII,
 C. J. Evans, L. Simard, and H. Takami, Eds., Society of Photo-Optical Instrumentation Engineers (SPIE) Conference Series 10702, 107021C (2018).
- [6] W. Taylor, M. Cirasuolo, J. Afonso, et al., "Rising MOONS: an update on the VLT's next multi-object spectrograph as it begins to grow," in Ground-based and Airborne Instrumentation for Astronomy VII, C. J. Evans, L. Simard, and H. Takami, Eds., Society of Photo-Optical Instrumentation Engineers (SPIE) Conference Series 10702, 107021G (2018).
- [7] M. Wolf, D. Adler, M. Bershady, et al., "A near infrared integral field spectrograph for the southern african large telescope (salt)," in Astronomical Telescopes + Instrumentation, (2018).
- [8] M. P. Smith, M. J. Wolf, M. A. Bershady, et al., "A Near Infrared Integral Field spectrograph (NIR) for the Southern African Large Telescope (SALT): mechanical design," in Ground-based and Airborne Instrumentation for Astronomy VII, C. J. Evans, L. Simard, and H. Takami, Eds., 10702, 1071 – 1083, International Society for Optics and Photonics, SPIE (2018).
- [9] E. B. Burgh, K. H. Nordsieck, H. A. Kobulnicky, et al., "Prime Focus Imaging Spectrograph for the Southern African Large Telescope: optical design," in *Instrument Design and Performance for Optical/Infrared Ground-based Telescopes*, M. Iye and A. F. M. Moorwood, Eds., Society of Photo-Optical Instrumentation Engineers (SPIE) Conference Series 4841, 1463–1471 (2003).
- [10] M. J. Wolf, A. I. Sheinis, M. P. Mulligan, et al., "Designing the optimal semi-warm NIR spectrograph for SALT via detailed thermal analysis," in *Ground-based and Airborne Instrumentation for Astronomy II*, I. S. McLean and M. M. Casali, Eds., 7014, 1084 – 1094, International Society for Optics and Photonics, SPIE (2008).
- [11] M. J. Wolf, A. I. Sheinis, T. B. Williams, et al., "Performance predictions for the Robert Stobie spectro-graph near infrared arm on SALT," in Ground-based and Airborne Instrumentation for Astronomy III, I. S. McLean, S. K. Ramsay, and H. Takami, Eds., 7735, 2822 2833, International Society for Optics and Photonics, SPIE (2010).
- [12] M. A. Bershady, D. R. Andersen, J. Harker, et al., "SparsePak: A formatted fiber field unit for the WIYN telescope bench spectrograph. i. design, construction, and calibration," Publications of the Astronomical Society of the Pacific 116, 565–590 (2004).
- [13] L. Crause, M. Bershady, and D. Buckley, "Investigation of focal ratio degradation in optical fibres for astronomical instrumentation," in *Ground-based and Airborne Instrumentation for Astronomy II*, I. S. McLean and M. M. Casali, Eds., **7014**, 2194 2204, International Society for Optics and Photonics, SPIE (2008).
- [14] N. Drory, N. MacDonald, M. A. Bershady, et al., "The MaNGA Integral Field Unit Fiber Feed System for the Sloan 2.5 m Telescope," The Astronomical Journal 149, 77 (2015).
- [15] J. R. P. Angel, M. T. Adams, T. A. Boroson, et al., "A very large optical telescope array linked with fused silica fibers.," 218, 776–782 (1977).
- [16] L. W. Ramsey, "Focal ratio degradation in optical fibers of astronomical interest.," in Fiber Optics in Astronomy, S. C. Barden, Ed., Astronomical Society of the Pacific Conference Series 3, 26–39 (1988).
- [17] E. Carrasco and I. R. Parry, "A method for determining the focal ratio degradation of optical fibres for astronomy," *Monthly Notices of the Royal Astronomical Society* **271**, 1–12 (1994).
- [18] A. D. Eigenbrot, M. A. Bershady, and C. M. Wood, "The impact of surface-polish on the angular and wavelength dependence of fiber focal ratio degradation," in *Ground-based and Airborne Instrumentation for Astronomy IV*, I. S. McLean, S. K. Ramsay, and H. Takami, Eds., 8446, 1822 – 1831, International Society for Optics and Photonics, SPIE (2012).
- [19] A. Eigenbrot and M. A. Bershady, "Vertical Population Gradients in NGC 891. I. ∇Pak Instrumentation and Spectral Data," 853, 114 (2018).
- [20] M. P. Smith, S. Chattopadhyay, A. Hauser, et al., "Development and characterization of a precisely adjustable fiber polishing arm," in Advances in Optical and Mechanical Technologies for Telescopes and Instrumentation IV, R. Navarro and R. Geyl, Eds., 11451, 1245 1251, International Society for Optics and Photonics, SPIE (2020).